

Redox Dynamics of Pt and Cu Nanoparticles on TiO₂ during the Photocatalytic Oxidation of Methanol under Aerobic and Anaerobic Conditions Studied by In Situ Modulated Excitation X-ray Absorption Spectroscopy

Gian Luca Chiarello,* Massimo Bernareggi, and Elena Selli



Cite This: *ACS Catal.* 2022, 12, 12879–12889



Read Online

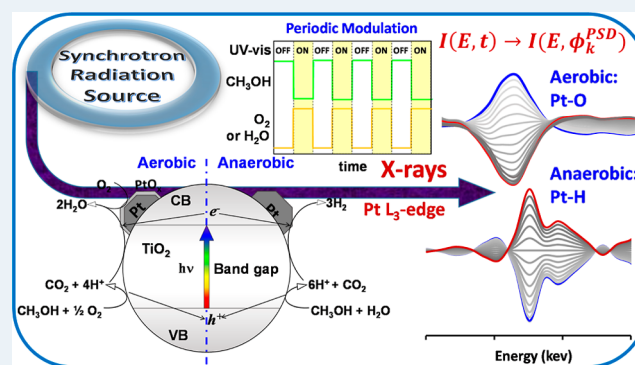
ACCESS |

Metrics & More

Article Recommendations

ABSTRACT: In situ modulated excitation X-ray absorption spectroscopy (ME-XAS) at the Pt L₃- and Cu K-edges has been successfully used in this work to shed light on the controversial role that Pt and Cu nanoparticles (NPs) on TiO₂ have in photocatalysis. TiO₂ photocatalysts, either bare or modified by Pt and Cu NPs, synthesized in a single step by flame spray pyrolysis, were tested in the gas-phase photocatalytic oxidation of methanol to CO₂ under both *aerobic* (CH₃OH + 3/2O₂ → CO₂ + 2H₂O) and *anaerobic* (CH₃OH + H₂O → CO₂ + 3H₂) conditions. Both Pt- and Cu-containing TiO₂ showed lower activity than bare TiO₂ under *aerobic* conditions, while higher H₂ and CO₂ production rates were attained under *anaerobic* conditions in the presence of the Pt co-catalyst, with copper-containing TiO₂ having in this case an activity similar to that of bare titania. ME-XAS, coupled with phase-sensitive detection, proved in fact that Pt NPs efficiently capture the electrons photopromoted in the conduction band of TiO₂ and are the active sites for H₂ or H₂O evolution under *anaerobic* or *aerobic* conditions, respectively. Much more complex is the role of Cu-NPs on titania, with ME-XAS revealing that copper is simultaneously present in different oxidation states, depending on the reaction conditions. Cu NPs are not the reaction active sites under *anaerobic* conditions, while a Cu(II)/Cu(I) redox switching occurs under chopped irradiation under *aerobic* conditions.

KEYWORDS: photocatalytic methanol oxidation, hydrogen production, in situ modulated excitation X-ray absorption spectroscopy, flame spray pyrolysis, Pt nanoparticles, Cu nanoparticles



1. INTRODUCTION

The activity of heterogeneous catalysts, including photocatalytic materials, is strongly affected by the structure, the oxidation state, and the redox dynamics of surface active sites, particularly when a key role is played by co-catalyst nanoparticles (NPs) dispersed over the support surface. For instance, titanium dioxide surface modification by metal NPs, able to capture photopromoted electrons, may lead to an increased photoactivity with respect to that of the bare material.^{1–3} However, the effect on photoactivity produced by the same metal NPs on the titania surface may largely depend on the reaction conditions, for example, if the modified photocatalyst is exploited in hydrogen production under *anaerobic* conditions or in the mineralization of organic pollutants under *aerobic* conditions.

Platinum NPs on the TiO₂ surface are known to increase the rate of hydrogen production from methanol photoreforming with respect to bare TiO₂,^{3–5} whereas Pt NPs can have either

limited beneficial^{6,7} or even detrimental effects in the photocatalytic oxidation of organics.⁸ Moreover, the oxidation state and the size distribution of metal NPs largely depend on the method employed to prepare the photocatalyst.^{9,10} Copper, which has been recently investigated as co-catalyst of TiO₂, being nontoxic and relatively inexpensive with respect to noble metals, can be present in different oxidation forms on the TiO₂ surface, either as Cu(II), Cu(I), or as metallic Cu, which are easily convertible one into the other, especially under irradiation. All of these different forms of copper may play completely different roles in photocatalysis.^{11,12}

Received: June 23, 2022

Revised: September 24, 2022

In this context, information on the surface redox dynamics occurring in metal NPs on the photocatalyst surface under real working conditions is crucial for understanding any catalyst structure versus activity relationship and getting a deeper insight into the photocatalytic reaction mechanism, which are of outmost importance for the design and development of novel and more active materials. Several operando spectroscopic techniques can be exploited to pursue this goal,^{13,14} including Fourier transform infrared spectroscopy (FTIR),^{15–17} diffuse reflectance infrared Fourier transform spectroscopy (DRIFTS),^{18–22} attenuated total reflectance (ATR),²³ nuclear magnetic resonance (NMR),²⁴ Raman spectroscopy,^{17,25,26} X-ray absorption spectroscopy (XAS),^{5,21,22,24,26–29} and X-ray diffraction (XRD).^{26,30} However, the main challenge consists in discerning between the signal contributions of active sites from the static signal due to the background, the bulk, and the spectator species. The exploitation of XAS delivers the intrinsic advantages of being element-specific, with a large penetration depth, and provides information on the local coordination and on the oxidation state of chemical elements.³¹ Moreover, X-ray absorption near-edge structure (XANES) spectroscopy is also sensitive to the adsorption of adsorbates, such as H, CO, O, or OH,³² affecting the local coordination around the absorber atoms at the surface. Moreover, the sensitivity to surface species can be significantly improved by the high-energy-resolution fluorescence detection (HERFD-XAS) technique,²¹ although it requires higher photon flux and is available only in few beamlines. Due to the low surface to bulk atomic ratio, the presence of adsorbates on the surface causes only subtle changes in the XANES spectrum, which can be extracted, for example, through the so-called $\Delta\mu$ XANES analysis procedure,³² consisting in the subtraction of the reference XANES spectrum of the bare metal from that of the metal in the presence of the adsorbate. The so-obtained difference spectrum is a “signature” of the nature of the adsorbate and provides information on the coverage and on the binding site geometry.

However, $\Delta\mu$ XANES spectroscopy presents some critical issues related to the difficulty of recording the reference spectrum of the bare metal and the need of smoothing the spectrum noise. Modulated excitation XAS (ME-XAS)^{30,33–36} represents a valid alternative to $\Delta\mu$ XANES, overcoming the above-mentioned drawbacks. ME-XAS is achieved through the cyclic variation of the experimental conditions (e.g., gas composition or concentration, pressure, pH, potential, irradiation, etc.),^{37,38} while recording time-resolved XAS spectra. The cycles are then merged into a single set of averaged time-resolved spectra with an improved signal to noise ratio. This can be applied only to fully reversible processes (such as catalytic reactions). ME-XAS exploits the phase-sensitive detection (PSD) algorithm to extract the response of the active species by filtering the signals of spectator species (including the background) and the noise.^{37,39} Hence, the obtained demodulated spectra are formally similar to difference spectra but have a significantly improved signal to noise ratio.

ME-XAS has been successfully employed to largely enhance the spectra quality and to highlight even tiny variations of oxidation state occurring in metal NPs (Pd, Pt, Rh, and Ru) under several modulation experiments of gas-phase composition switch, such as CO vs NO,³³ H₂ vs O₂,⁴⁰ and CH₄ versus

O₂.⁴¹ Gaur et al. probed the active sites of MoS₂ catalysts by MES-XAS under H₂O vs H₂S modulation.²⁸

In this work, ME-XAS has been exploited in the in situ study of the surface dynamics of Pt or Cu NPs deposited on TiO₂ during the photocatalytic oxidation of methanol to CO₂ under either *aerobic* (2CH₃OH + 3O₂ → 2CO₂ + 4H₂O) or *anaerobic* (CH₃OH + H₂O → CO₂ + 3H₂) conditions. By this way, a deeper insight has been obtained on the reaction mechanisms involving Pt and Cu NPs on TiO₂ under irradiation in the presence of O₂ or H₂O vapor and on the origin of their effects on photoactivity with respect to bare TiO₂.

2. EXPERIMENTAL SECTION

2.1. Photocatalysts Synthesis. The bare (FP-TiO₂) and metal NP-modified TiO₂ powders (FP-Pt/TiO₂ and FP-Cu/TiO₂) were prepared in a single step by flame spray pyrolysis (FP).⁴² All chemicals were purchased from Sigma-Aldrich and used as received. 50 mL of 0.6 M titanium tetraisopropoxide in xylene solution was mixed with 25 mL of propanoic acid eventually containing the proper amount of Cu or Pt precursors (copper acetate monohydrate or hexachloroplatinic acid) in order to have a final nominal 2 wt % metal loading on TiO₂. Such a relatively high metal loading was chosen in order to improve the time-resolved XAS spectra quality. The so-obtained solutions were injected into the burner nozzle at 4 mL min^{−1} by means of a syringe pump, sprayed with 5.0 L min^{−1} of O₂ and burned through a methane/oxygen flame ring (1.0 and 2.0 L min^{−1} flow rates for CH₄ and O₂, respectively). The so-produced powders were collected on glass fiber filters (Whatman) placed above the burner.

2.2. Photocatalyst Characterization. The effective Cu or Pt loading of FP-Cu/TiO₂ and FP-Pt/TiO₂ powders was determined by inductively coupled plasma (ICP) analysis employing a Perkin Elmer Optima 8000 IPC-OES apparatus after their complete dissolution in 10 mL of aqua regia (3:1 HCl/HNO₃ molar ratio) and 2.5 mL of saturated HF solutions at 378 K for 4 h. Alternatively, the samples were treated with hot aqua regia only (no hydrofluoric acid) to dissolve surface Cu or Pt only. The obtained suspension was filtered to remove the undissolved oxide and then analyzed. The BET specific surface area (SSA) was measured by N₂ adsorption at 77 K with an ASAP 2020 apparatus after out-gassing in vacuo at 150 °C for at least 2 h. XRD patterns were recorded using the copper K α radiation (λ = 1.54056 Å) in a Philips PW3020 powder diffractometer, operating at 40 kV and 40 mA. Phase analysis was performed using the “*Quanto*” software,⁴³ applying the Rietveld refinement method.⁴⁴ The mean anatase and rutile crystallite size was estimated through the Scherrer equation⁴⁵ from the full width of half-maximum value of the most intense reflections (2θ = 25.4° and 2θ = 27.4° for the anatase and rutile phases, respectively).

UV–vis diffuse reflectance spectra were recorded with a Jasco V-670 spectrophotometer equipped with a PIN-757 integrating sphere using barium sulfate as the blank. The spectra are reported as both absorption (*A*) spectra ($A = 1 - R$, *R* being the reflectance) and Tauc plots of the Kubelka–Munk transform to estimate the band gap.

2.3. Photocatalytic Tests. The photocatalysts were tested in the gas-phase photocatalytic oxidation of methanol under either *aerobic* or *anaerobic* conditions. In the former case, the photoreactor was fed with a 3.6% CH₃OH/3.8% H₂O/N₂ gas stream (photo-steam reforming reaction); in the latter case, the photoreactor was fed with 18% CH₃OH/20% O₂/N₂. The gas

Table 1. Characterization of the As-Prepared Flame-made Samples: Metal Loading Obtained by ICP-OES, SSA, Crystalline Phase Distribution, Anatase (d_a) and Rutile (d_r) Crystallite Average Size, and Band Gap Values of the Investigated Photocatalysts

sample	Pt or Cu (wt %)	SSA ($\text{m}^2 \text{g}^{-1}$)	anatase (%)	d_a (nm)	rutile (%)	d_r (nm)	band gap (eV)
FP-TiO ₂		110	86.1	14.4	13.9	9.3	3.12
FP-Pt/TiO ₂	1.61	151	86.3	14.1	13.7	16.6	3.15
FP-Cu/TiO ₂	1.92	132	77.3	26.8	22.7	16.5	3.05

stream was obtained by bubbling 60 mL min⁻¹ pure N₂ into a 20 vol % CH₃OH in H₂O solution kept at 30 °C or 60 mL min⁻¹ synthetic air in pure methanol kept at 0 °C. The amount of methanol and water vapors in the obtained gas stream were calculated with AVEVA PRO/II Simulation software for a non-ideal solution. The gas flow rate was controlled by means of a mass flow meter (EL-FLOW Base, Bronkhorst).

The photocatalytic tests were performed using a stainless-steel setup similar that described elsewhere⁴⁶ but operating in the continuous gas flow feeding mode. The photocatalyst powder (15 mg) was dispersed onto *ca.* 7 g of 20–40 mesh (0.42–0.85 mm) quartz grains by adding a few droplets of water, followed by mixing and drying in an oven at 70 °C for at least 1 h. The so-obtained photocatalytic bed was then loaded into a home-made stainless-steel photoreactor (50 mm diameter and 2 mm depth), closed with a Pyrex glass optical window with a *ca.* 320 nm cutoff edge. The outlet of the photoreactor was connected on-line to a gas chromatograph (Agilent 6890N) through a six-way injection valve, followed by a bubbler filled with a NaHCO₃/Na₂CO₃ aqueous solution acting as a trap of photoproducted formic acid and formaldehyde.

The gas chromatograph was equipped with two capillary columns (MoleSieve 5A and HP-Plot U), two detectors (thermal conductivity detector and flame ionization detector), and a Ni-based catalyst for CO and CO₂ methanation. Prior to any analysis, the system was thoroughly purged with pure N₂ for 20 min in the dark (in the case of the steam reforming reaction, to remove any trace of O₂) or with air. The irradiation source was a 300 W Xenon arc lamp (LOT-qd) placed at 20 cm from the reactor. The irradiation intensity on the reactor was 120 mW cm⁻² as measured with a calibrated Thorlabs S130VC photodiode. The photoreactor was irradiated for 190 min during a typical run, while the gas-phase composition was monitored by gas chromatography (GC) analysis, starting 2 min after the beginning of irradiation and then at 19 min intervals.

The overall amount of produced formic acid was determined at the end of the run by ion chromatography analysis of the aqueous solution contained in the trap using a Metrohm 761 Compact IC instrument. Formaldehyde was determined by the Nash method.^{47,48} Briefly, after dilution, the solution contained in the trap flask was added to an equivalent volume of Nash's reagent (25 g of ammonium acetate, 2.1 mL of acetic acid, and 0.2 mL of acetylacetone, dissolved in ultrapure water, up to 100 mL total volume) and stirred for 1 h. Formaldehyde concentration was determined by spectrophotometric analysis at 413 nm after calibration.

2.4. ME-XAS Experiments. Time-resolved XAS spectra were recorded in the energy-dispersive mode at either the Cu K-edge (8979 eV) or the Pt L3-edge (11,564 eV) at the ID24 beamline of ESRF in Grenoble (France). The experiments were performed using a 1.5 mm quartz capillary in situ cell.⁴⁹ The photocatalyst powder was placed at the center of the

capillary, fixed between two quartz flakes, and then connected to the gas manifold. A 300 W Xe arc lamp connected to a water filter, an automatic shutter, and a liquid light guide (all purchased by Quantum Design Europe) was employed to irradiate the photocatalyst bed with UV–vis light. The water filter helps to keep the temperature of the catalyst constant during the experiment because it removes the IR region of the incident spectrum. Two modulation experiments were performed, switching the gas atmosphere from 3.6% CH₃OH/He in the dark to (i) 5% O₂/He under UV–vis irradiation or to (ii) 3.8% H₂O/He under UV–vis irradiation. By this way, methanol pre-absorbed on the photocatalyst in the dark reacted with oxygen (aerobic conditions) or with water (anaerobic conditions) under UV–vis irradiation. Inlet water and methanol vapor flows were attained by bubbling He in each of the two liquids. An automatic four-way valve was employed to switch the inlet gas composition. The composition of the outlet gas from the capillary was continuously monitored by means of an OmniStar Pfeiffer Vacuum mass spectrometer (MS).

Prior to the modulation experiment, the set up was purged with He (40 mL min⁻¹) under dark conditions until the O₂ ($m/Z = 32$) and N₂ ($m/Z = 28$) MS signals were stable. A total of 40 consecutive time-resolved XAS spectra (5 s per spectrum) were recorded in each 200 s-long modulation period, which consisted of 20 XAS spectra recorded under CH₃OH in the dark and 20 XAS spectra recorded under O₂ (or H₂O) under UV–vis irradiation. Both the switching four-way valve and the shutter of the Xe lamp were synchronized with XAS spectra acquisition. A full ME-XAS experiment consisted in 15 consecutive modulation periods.

The averaged time-resolved and PSD transformed (phase-resolved) spectra were obtained using a MATLAB routine. The first five modulation periods were always discarded to ensure that steady-state conditions were achieved.

3. RESULTS AND DISCUSSION

3.1. Photocatalyst Characterization. The same 1.61 wt % Pt loading in the FP-Pt/TiO₂ photocatalyst was obtained by ICP–optical emission spectroscopy (ICP-OES) elemental analyses (Table 1) after dissolving either the whole powder or the surface Pt only. This demonstrates that Pt NPs are on the photocatalyst surface and not in the TiO₂ bulk. On the other hand, a 1.92 wt % copper loading was obtained after complete FP-Cu/TiO₂ dissolution, but when the TiO₂ support was not dissolved, the amount of copper determined by ICP-OES analysis was 1.49 wt %. This indicates that copper is in part within the titanium dioxide bulk. Indeed, the Cu(II) radius, 0.87 Å, is only slightly larger than the Ti(IV) radius, 0.745 Å. Thus, copper may partially substitute titanium in the lattice⁵⁰ during the one-step flame synthesis.

The XRD patterns identify anatase as the main crystallographic phase of the three flame-made TiO₂ photocatalysts (Table 1), as already observed with similar materials with

lower metal loading.⁵¹ No reflections related to copper or platinum, in either the oxide or metal form, could be detected due to the low metal loading. The presence of Pt had almost no effect on the phase composition of the material, while copper slightly promoted the formation of rutile during the single-step synthesis. Indeed, doping TiO₂ with Cu(II) may generate oxygen vacancies inside the crystalline structure, resulting in a favored growth of rutile crystallites.^{50,52,53}

Bare TiO₂ possesses a high SSA of 110 m² g⁻¹, typical of flame-made powders. The addition of Cu and Pt during the flame synthesis led to larger SSA values (132 and 151 m² g⁻¹, respectively, see Table 1), despite the larger crystallite size. Thus, the presence of metal NPs appears to reduce crystallite aggregation.

The UV–vis absorption spectrum of FP-TiO₂, reported in Figure 1a, shows the usual profile of flame-made bare TiO₂ with an absorption threshold below 400 nm.

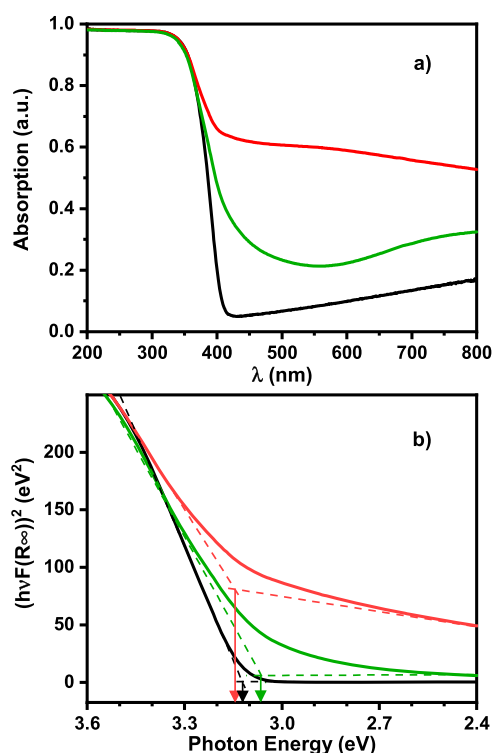


Figure 1. (a) Absorption spectra and (b) Tauc plots of the Kubelka–Munk transform of FP-TiO₂ (black lines), FP-Pt/TiO₂ (red lines), and FP-Cu/TiO₂ (green lines).

As expected, in the case of FP-Pt/TiO₂, an extended absorption is present in the visible range, compatible with the dark-gray color of this sample. The absorption spectrum of FP-Cu/TiO₂ exhibits the d–d transition in the 600–800 nm range typical of stable oxidized copper in the Cu_xO form. The extra absorption tail at 400–500 nm can be ascribed to interfacial charge transfer (IFCT), resulting in the reduction of Cu(II) to Cu(I) by electrons photopromoted directly from the valence band (VB) of TiO₂.^{52,54–56}

The band gap of the three photocatalysts, estimated from the Tauc plot of the Kubelka–Munk transform, as shown in Figure 1b, are very similar, that is, 3.12 and 3.15 eV, respectively, for bare and Pt-modified TiO₂, while a slightly narrower band gap of 3.05 eV is obtained for FP-Cu/TiO₂, in line with its larger rutile content and to partial Cu doping.^{57,58}

3.2. Photocatalytic Activity. **3.2.1. Anaerobic Conditions.** In the photo-steam reforming reaction ($\text{CH}_3\text{OH} + \text{H}_2\text{O} \rightarrow \text{CO}_2 + 3\text{H}_2$) under *anaerobic* conditions, methanol is oxidized up to carbon dioxide through a consecutive reaction paths, implying the formation of carbon monoxide, formaldehyde, and formic acid as main intermediates, with the simultaneous production of hydrogen.^{5,23} The production of hydrogen and by-products increased within the first 20 min of irradiation and then stabilized (Figure 2).

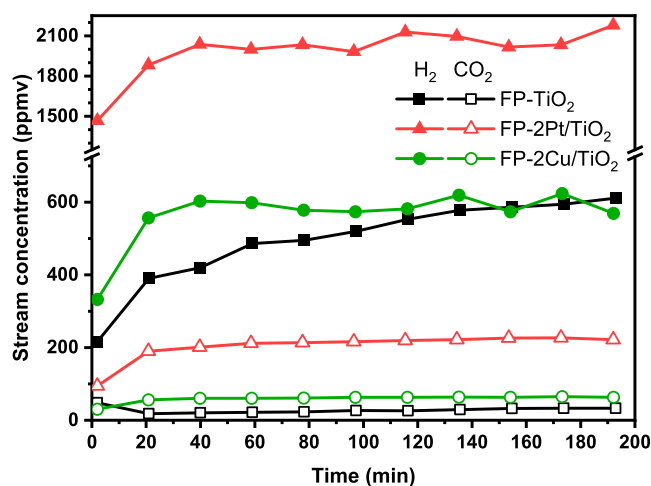


Figure 2. Time-on-stream concentration profiles of hydrogen (full symbols) and carbon dioxide (void symbols) obtained with FP-TiO₂ (black squares), FP-Pt/TiO₂ (red triangles), and FP-Cu/TiO₂ (green circles).

FP-Pt/TiO₂ is by far the best performing photocatalyst in this reaction, with a hydrogen production rate r_{H_2} of ca. 19 mmol h⁻¹ g_{cat}⁻¹. Platinum is a very effective co-catalyst of TiO₂,³ mainly because it is able to capture photopromoted electrons due to its higher work function with respect to that of TiO₂ (5.12–5.93 vs 4.6–4.7 eV, respectively), with a consequent better separation of photoproduced charge carriers. The difference in work function is the driving force for electron transfer at the metal/semiconductor interface: the larger the difference, the more efficient is the electron transfer. Moreover, proton reduction to H₂ proceeds more efficiently on Pt than on the TiO₂ surface.

By contrast, a significantly lower r_{H_2} value was obtained with FP-Cu/TiO₂, just slightly higher than that attained with FP-TiO₂ (Table 2). Indeed, the work function of Cu (4.53–5.1 eV) is very close to that of TiO₂; thus, electron transfer to copper is much less efficient than to platinum. It is worth underlining, however, that maximum photocatalytic activity is usually attained at Cu and Pt loadings lower than those adopted here,⁶ which were chosen to have sufficiently high signals in the in situ ME-XAS analysis.

Under these reaction conditions, methanol is only partially oxidized up to CO₂ with a selectivity (S_{CO_2}) that doubles up to 32% upon metal NP modification of TiO₂ and a parallel decrease of selectivity to CO (Table 2). The selectivity is calculated with respect to r_{H_2} considering that 3 mol of H₂ per mole of CO₂ (i.e., $S_{\text{CO}_2} = 3 \times 100 \cdot r_{\text{CO}_2} / r_{\text{H}_2}$), 2 mol of H₂ per mole of CO and HCO₂H, and 1 mol of H₂ per mole of H₂CO are produced. Formaldehyde was the main product of

Table 2. Production Rates of and Selectivity to Hydrogen, Carbon Dioxide, Carbon Monoxide, Formaldehyde, and Formic Acid in the Anaerobic Oxidation of Methanol over the Investigated Flame-made Photocatalysts

sample	production rates (mmol h ⁻¹ g _{cat} ⁻¹)					% selectivity			
	<i>r</i> _{H₂}	<i>r</i> _{CO₂}	<i>r</i> _{CO}	<i>r</i> _{H₂CO}	<i>r</i> _{HCOOH}	<i>S</i> _{CO₂}	<i>S</i> _{CO}	<i>S</i> _{H₂CO}	<i>S</i> _{HCOOH}
FP-TiO ₂	4.94	0.26	0.21	2.87	0.43	15.8	8.5	58.1	17.4
FP-Pt/TiO ₂	19.25	2.06	0.06	8.62	1.72	32.1	0.6	44.8	17.9
FP-Cu/TiO ₂	5.02	0.54	0.06	2.79	0.35	32.3	2.4	55.6	13.9

methanol oxidation with all three investigated photocatalysts, with a selectivity above 45%, while the selectivity to formic acid was less affected by the presence of metal NPs (Table 2). The sum of the selectivity values to CO₂, CO, H₂CO, and HCOOH attained with the three photocatalysts is close to 100%, which demonstrates that other possible products, for example, dimethyl ether, are not directly involved in H₂ production.

3.2.2. Aerobic Conditions. As shown in Table 3, bare FP-TiO₂ was the most active photocatalyst in the photocatalytic

Table 3. Rates of Carbon Dioxide, Carbon Monoxide, Formaldehyde, Formic Acid, and Methane Production in the Aerobic Oxidation of Methanol with the Investigated Flame-made Photocatalysts

sample	production rates (mmol·h ⁻¹ ·g _{cat} ⁻¹)				
	<i>r</i> _{CO₂}	<i>r</i> _{CO}	<i>r</i> _{H₂CO}	<i>r</i> _{HCOOH}	<i>r</i> _{CH₄}
FP-TiO ₂	6.01	0.49	27.95	3.08	0.27
FP-Pt/TiO ₂	3.35	n.d.	17.61	4.85	0.31
FP-Cu/TiO ₂	0.82	0.08	8.01	0.80	0.37

oxidation of methanol in the presence of O₂, especially in terms of CO₂ and formaldehyde production, with the latter being the main product of methanol oxidation in this case as well. CH₄ and CO were also detected as side products. The overall photocatalytic activity, expressed as the sum of the production rates of all C-containing species, under aerobic conditions was significantly higher than that under anaerobic conditions, increasing from 4 to 38 mmol h⁻¹ g_{cat}⁻¹ for bare TiO₂, from 12 to 26 mmol h⁻¹ g_{cat}⁻¹ for FP-Pt/TiO₂, and from 4 to 10 mmol h⁻¹ g_{cat}⁻¹ for FP-Cu/TiO₂. Pt NPs on TiO₂ had beneficial effects in formic acid production, while Cu NPs caused a dramatic drop of the overall photoactivity compared to bare TiO₂.

Hence, under aerobic conditions, the here adopted relatively high Pt and Cu NP loading on TiO₂ leads to a lower photocatalytic activity with respect to bare TiO₂. Moreover, surface TiO₂ modification with Cu and Pt NPs has opposite effects on methanol oxidation in the presence of water vapor or of oxygen. In fact, in the presence of water, Cu and Pt NPs on TiO₂ increase the rate of CO₂ production, whereas they have detrimental effects in the presence of oxygen, with bare TiO₂ exhibiting under such conditions a significantly higher CO₂ production rate than both metal-modified photocatalysts.

3.3. Pt L3-Edge ME-XAS Experiments. The XANES spectrum at the Pt L3-edge recorded with as-prepared FP-Pt/TiO₂ exhibits an intense white line (Figure 3), indicating that Pt is prevalently in the oxidized form (Table 4). However, after both modulation experiments, either in the presence of vapor or in the presence of oxygen, the intensity of the white line significantly decreases, indicating that Pt undergoes reduction under UV-vis irradiation.

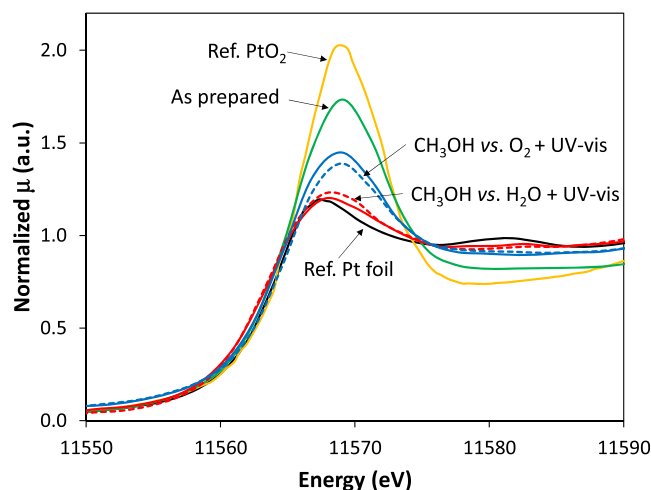


Figure 3. XANES spectra at the Pt L3-edge recorded with FP-Pt/TiO₂: last averaged spectrum recorded under 3.6% CH₃OH/He in the dark (dashed lines) and under 3.8% H₂O/He (or 5% O₂/He) and irradiation (continuous lines) during the modulation experiments in the presence of oxygen (blue lines) and of water vapor (red lines) under irradiation. The XANES spectra of as-prepared FP-Pt/TiO₂ (green line), of reference PtO₂ (orange line), and of a Pt foil (black line) are reported for comparison.

Table 4. Results of the Linear Combination Analysis of the XANES Spectra at the Pt L3-Edge Recorded with FP-Pt/TiO₂ as Prepared and during the CH₃OH vs O₂ + Light Modulation Experiment

XANES spectrum	Pt(IV) (%)	Pt(0) (%)
as prepared	54	46
under 3.6% CH ₃ OH/He in the dark	12	88
under 5% O ₂ /He + light	15	85

In particular, in the photo-steam reforming reaction (anaerobic conditions), Pt undergoes almost complete reduction, as already observed in previous studies,⁵ with the white line intensity of the averaged time-resolved spectra clearly resembling that of reference metallic Pt (red compared to black lines in Figure 3). By contrast, in the presence of O₂ (aerobic conditions), the linear combination fitting of the last averaged spectrum measured under CH₃OH/He using the XANES spectra of a Pt foil and PtO₂ as standards reveals the presence of ca. 12% residual Pt(IV), which slightly increases to 15% under UV-vis irradiation in the presence of O₂ (Table 4). Considering the high surface dispersion of Pt (i.e., a relatively high surface to bulk Pt atomic ratio), this variation of Pt(IV) content is consistent with surface Pt atom oxidation in contact with oxygen under UV-vis irradiation, followed by reduction during the subsequent switch to methanol vapor.

Earlier work from Teoh et al. has already highlighted the occurrence of redox dynamics involving Pt(0), Pt(II), and

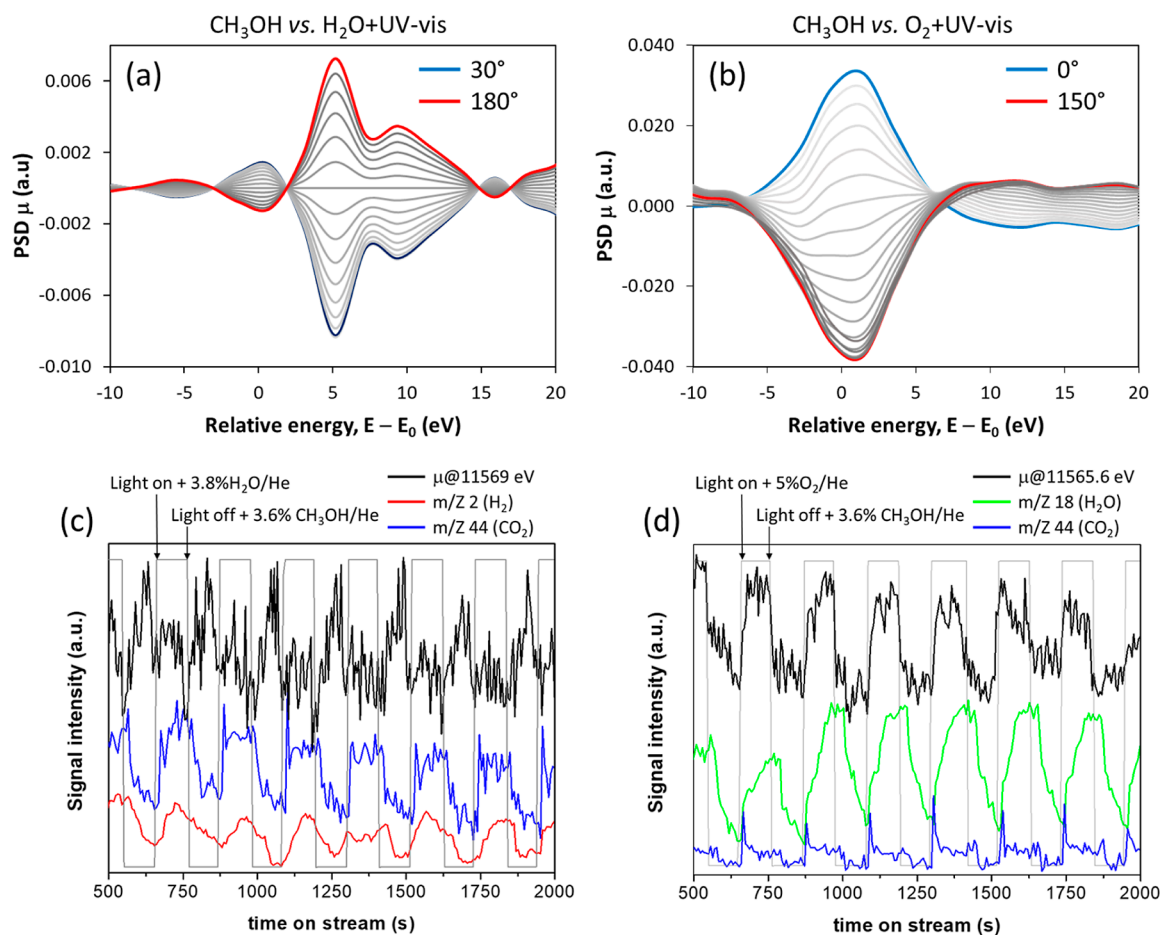


Figure 4. ME-XANES results at the Pt L3-edge obtained with FP-Pt/TiO₂. (a,b) Phase-resolved spectra in the $0^\circ < \varphi^{\text{PSD}} < 180^\circ$ range; (c,d) time-on-stream variation of the mass spectrometer m/Z signals of H₂ (red line), CO₂ (blue lines), and H₂O (green line) and of XAS absorption (μ , black line) at (c) 11,569 and (d) 11,565.6 eV in (a,c) CH₃OH vs H₂O + light and (b,d) CH₃OH vs O₂ + light modulation experiments.

Pt(IV) over flame-made Pt/TiO₂ during methanol photocatalytic mineralization as determined by ex situ XPS analysis.⁵⁹

During a modulation experiment, the system reversibly oscillates between two boundary states, reaching a steady-state condition. Thus, the last averaged time-resolved XANES spectrum recorded in the presence of methanol and the last spectrum recorded in the presence of O₂ (or in H₂O) under UV-vis irradiation provide information on the oxidation state and local structure of Pt NPs in these two boundary states. In particular, comparing the last XANES spectrum recorded under CH₃OH/He in the dark (dashed red and blue lines in Figure 3) with the last XANES spectrum recorded under irradiation in contact with water vapor (continuous red line) or oxygen (continuous blue line), a reversible variation of the XANES spectrum shape is observed. This spectrum variation can be highlighted applying the PSD algorithm, which transforms the averaged time-resolved XANES spectra into a set of phase-resolved XANES spectra (Figure 4a and b), with a typical envelope-like shape due to the sinusoidal signal intensity variation as a function of the demodulation angle (φ^{PSD}).³⁷ Phase-resolved spectra are essentially difference spectra with a significantly improved signal to noise ratio,³⁴ and their interpretation is similar to that of the spectra obtained by the $\Delta\mu$ -XANES technique.³²

The phase-resolved spectra obtained during the CH₃OH vs H₂O + light experiment (Figure 4a) exhibit a pronounced

variation at 5 eV and 10 eV above the Pt L3-edge energy. The shape of these spectra is very similar to that of the $\Delta\mu$ -XANES spectra reported by Teliska et al. and attributed to H adsorption on Pt by DFT calculations.⁶⁰ In particular, the positive variation at 5 eV is characteristic of H adsorbed on the atop (1-fold coordination), while that at 10 eV is due to H adsorbed on the fcc (3-fold coordination) sites of Pt.

Figure 4c shows the periodic and reversible time-resolved variation of the X-ray absorption (μ) at 11,569 eV (μ at 11,569 eV) (i.e., at 5 eV above the Pt L3-edge) in comparison with that of the mass spectrometer signals of H₂ ($m/Z = 2$) and CO₂ ($m/Z = 44$), which are the two main products of the $\text{CH}_3\text{OH} + \text{H}_2\text{O} \rightarrow \text{CO}_2 + 3\text{H}_2$ reaction under anaerobic conditions. The periodic production of H₂ and CO₂ occurred under the UV-vis irradiation semi-period in the presence of water over FP-Pt/TiO₂ pre-saturated with methanol vapor. The product evolution was accompanied by similar periodic decreases of X-ray absorption at 11,569 eV. A decrease of μ at 11,569 eV indicates a decreased H coverage over the Pt surface occurring under UV-vis irradiation due to H₂ formation and desorption. Hence, present ME-XAS results provide experimental evidence that Pt, acting as a collector of photo-promoted electrons, is the active site for hydrogen evolution.

On the other hand, the phase-resolved spectra obtained during the CH₃OH vs O₂ + light experiment (Figure 4b), that is, under aerobic conditions, exhibit a completely different shape and opposite variation with respect to those recorded

under *anaerobic* conditions (Figure 4a). The obtained phase-resolved spectra are very similar to the $\Delta\mu$ -XANES predicted by Teliska et al. by DFT calculation for O adsorption on a 2-fold bridged Pt site.⁶¹ Furthermore, Figure 4d shows that the μ signal at 11,565.6 eV (i.e., at 1.6 eV above the Pt L3-edge) periodically increases (i.e., with increasing Pt surface O coverage) under UV–vis irradiation in the presence of O₂, together with the production of H₂O and CO₂, in line with the CH₃OH + 3/2O₂ → CO₂ + 2H₂O reaction. Hence, in situ ME-XAS results confirm that also in this case, Pt is an active reaction site for oxygen absorption and water formation under *aerobic* conditions.

Based on these results, the mechanism of photocatalytic methanol oxidation on Pt/TiO₂ under both *aerobic* and *anaerobic* conditions is schematically reported in Figure 5. In

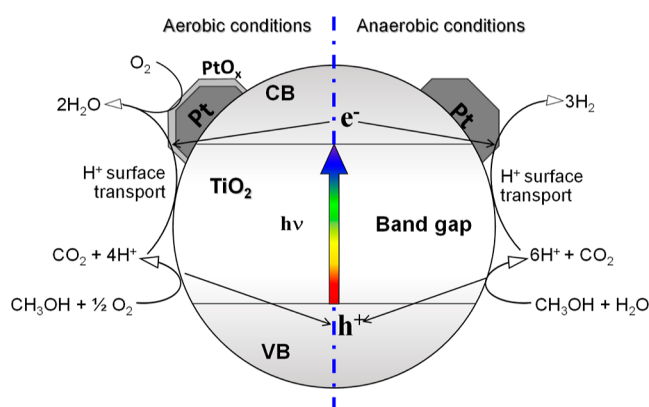
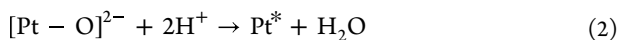
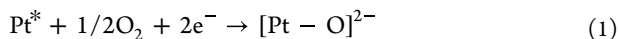


Figure 5. Mechanism of photocatalytic methanol oxidation under *aerobic* (CH₃OH + O₂) and *anaerobic* (CH₃OH + H₂O) conditions over Pt/TiO₂, as suggested by ME-XAS results.

both cases, methanol reacts on the TiO₂ surface with both photoproduced VB holes and H₂O or O₂ yielding H⁺ and CO₂. Protons can diffuse over the titania surface and reach Pt NP sites. Proton transport on the oxide surface primarily proceeds through hopping between water molecules in the chemisorbed and physisorbed water layers according to the Grotthuss mechanism.⁶² Under *anaerobic* conditions, protons undergo reduction to molecular hydrogen by photopromoted electrons transferred to Pt NPs from the TiO₂ conduction band (CB).

On the other hand, under *aerobic* conditions, a two-step multi-electron reduction of oxygen on the Pt surface occurs as deduced by our ME-XAS results (Figure 4b)



where Pt* is the surface active site and [Pt–O]^{2–} represents the oxidized Pt surface negatively charged. Hydroxyl radicals and superoxide radical anions are the typical reactive species involved in photocatalytic oxidation processes in the liquid phase. However, in the gas phase, any ionic intermediate species has to necessarily exist adsorbed on the catalyst surface where all reactions occur. Equation 1 represents the reaction involving oxygen as the electron acceptor species. Reaction 2 is likely the rate-determining step. Figure 4d corroborates this conclusion. In fact, under UV–vis irradiation, the XAS absorption at 11,565.6 eV readily increases, indicating a fast increase of O coverage with a simultaneous pick of CO₂ production (methanol is an efficient hole scavenger) and a

slower H₂O evolution. Hence, under *aerobic* conditions, the beneficial effect of Pt NPs able to capture photopromoted electrons is counterbalanced by the slow water evolution step (3), leading to a lower overall photocatalytic performance of Pt/TiO₂ with respect to bare TiO₂ (Table 2).

3.3.1. Cu K-Edge ME-XAS Analysis. Cu K-edge XANES spectra are characterized by the presence of a pre-edge peak due to the electron transition from the core 1s to the unoccupied 4p orbital of copper. The pre-edge position and intensity depend on the oxidation state of copper and on its coordination symmetry including the nature of the ligand.

For simplicity, Figure 6 shows only the 20th (i.e., the last spectrum measured under CH₃OH/He flow in the dark,

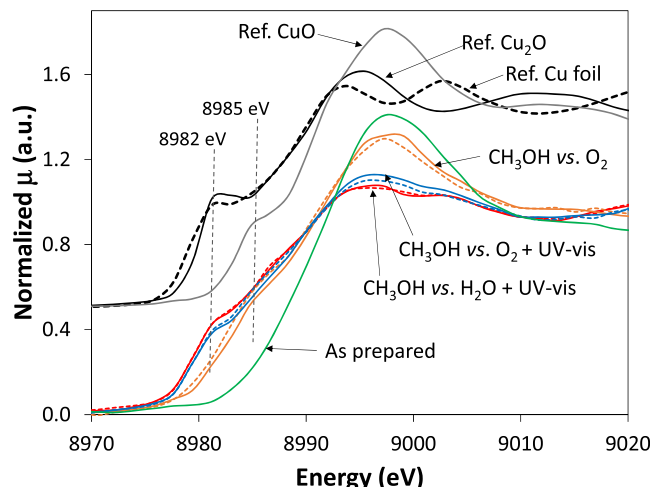


Figure 6. XANES spectra at the Cu K-edge of FP-Cu/TiO₂: last averaged spectra recorded under 3.6% CH₃OH/He in the dark (dashed lines) and under 3.8% H₂O/He or 5% O₂/He (continuous lines) during CH₃OH vs O₂ (orange lines), CH₃OH vs O₂ + light (blue lines), and CH₃OH vs H₂O + light (red lines) modulation experiments. The XANES spectra recorded with as-prepared FP-Cu/TiO₂ (green line) and with reference CuO, Cu₂O, and Cu foil are reported for comparison.

dashed lines) and 40th [i.e., the last spectrum measured under H₂O (or O₂)/He flow, continuous lines] averaged time-resolved XANES spectra of each modulation experiment, together with those of reference CuO, Cu₂O, and Cu foil.

The pre-edge of the reference materials shifts toward higher energy with increasing Cu oxidation state, from 8982 eV of Cu(0) and Cu(I) to 8985 eV of Cu(II), together with an increase of the white line intensity. The XANES spectrum of as-prepared FP-Cu/TiO₂ exhibits no pre-edge, which is typical of amorphous CuO NPs on titania,^{12,63} and an intense white line indicating that Cu is fully oxidized to Cu(II), as also confirmed by the linear combination analysis results reported in Table 5.

In their study on the photocatalytic oxidation of 2-propanol on Cu(II)-grafted TiO₂, Irie et al. suggested^{12,64} that electrons in the VB of TiO₂ can be photopromoted to reduce Cu(II) to Cu(I) through IFCT. However, from a thermodynamic point of view, the Cu(II)/Cu(I) switch can occur in presence of methanol (as reducer) and oxygen (as oxidizer) in the dark as well. Indeed, the standard reduction potential of Cu(II)/Cu(I) (0.16 V) is more positive than that of CO₂/CH₃OH (0.03 V). Thus, in order to discern the effect of light on the Cu(II)/Cu(I) redox dynamics, we performed an additional modulation

Table 5. Results of the Linear Combination Analysis of XANES Spectra at the Cu K-Edge Recorded with FP-Cu/TiO₂ as Prepared and Averaged Time-Resolved Spectra Recorded during Various Modulation Experiments

modulation experiment	XANES spectrum	Cu(II) (%)	Cu(I) (%)	Cu(0) (%)
as-prepared sample	in air	100		
CH ₃ OH vs O ₂ (dark)	under CH ₃ OH	42	58	
	under O ₂	54	46	
CH ₃ OH vs O ₂ + light	under CH ₃ OH	13	29	58
	under O ₂ + light	20	21	59
CH ₃ OH vs H ₂ O + light	under CH ₃ OH	6	24	70
	under H ₂ O + light	6	23	71

experiment of CH₃OH vs O₂ only in the dark (Figure 6 and Table 5). The results of the linear combination analysis reported in Table 5 confirm that 58% of Cu(II) is reduced to Cu(I) when it is exposed to pure methanol vapor and it is partially oxidized back to Cu(II) by oxygen in the dark. Moreover, we observed the appearance of the pre-edge feature at 8985 eV of Cu(II) (orange vs green line in Figure 6), indicating a surface rearrangement and crystallization of the CuO NPs consequent to the periodic switch of the gas phase composition. However, this material has no catalytic activity in methanol oxidation in the dark at room temperature. Thus,

this redox dynamics cannot be considered as an active catalytic cycle.

The same modulation experiment, but under periodic UV–vis irradiation during the oxygen semi-period (CH₃OH vs O₂ + light), demonstrates that light has a strong reducing effect on copper. Indeed, the linear combination analysis (see Table 5) indicates that *ca.* 60% of copper is reduced to Cu(0) under these conditions, whereas no Cu(0) formation was observed when the experiment was performed in the dark only. The copper reduction promoted by UV–vis light can be attributed to the IFCT of electrons photopromoted directly from the TiO₂ VB. The high Cu(0) percentage may suggest the formation of metal core–oxide shell NPs, although the presence of isolated CuO_x NPs cannot be excluded. A Cu(II)/Cu(I) redox dynamics is observed in this case as well (see Table 5), where Cu(II) periodically increases from 13 to 20% under O₂ + light. However, the lower Cu(II) content increase attained in contact with O₂ under UV–vis irradiation (7% increase) with respect to dark conditions (12% increase) can result from the partial reducing effect of IFCT in contrast with the oxidizing effect of O₂. The Cu(II)/Cu(I) redox dynamics under aerobic conditions and UV–vis irradiation is further confirmed by the phase-resolved XANES spectra shown in Figure 7b. In particular, two opposite variations are observed in the 0–15 and 15–30 eV regions above the Cu K-edge, corresponding to a shift of the edge toward higher energy

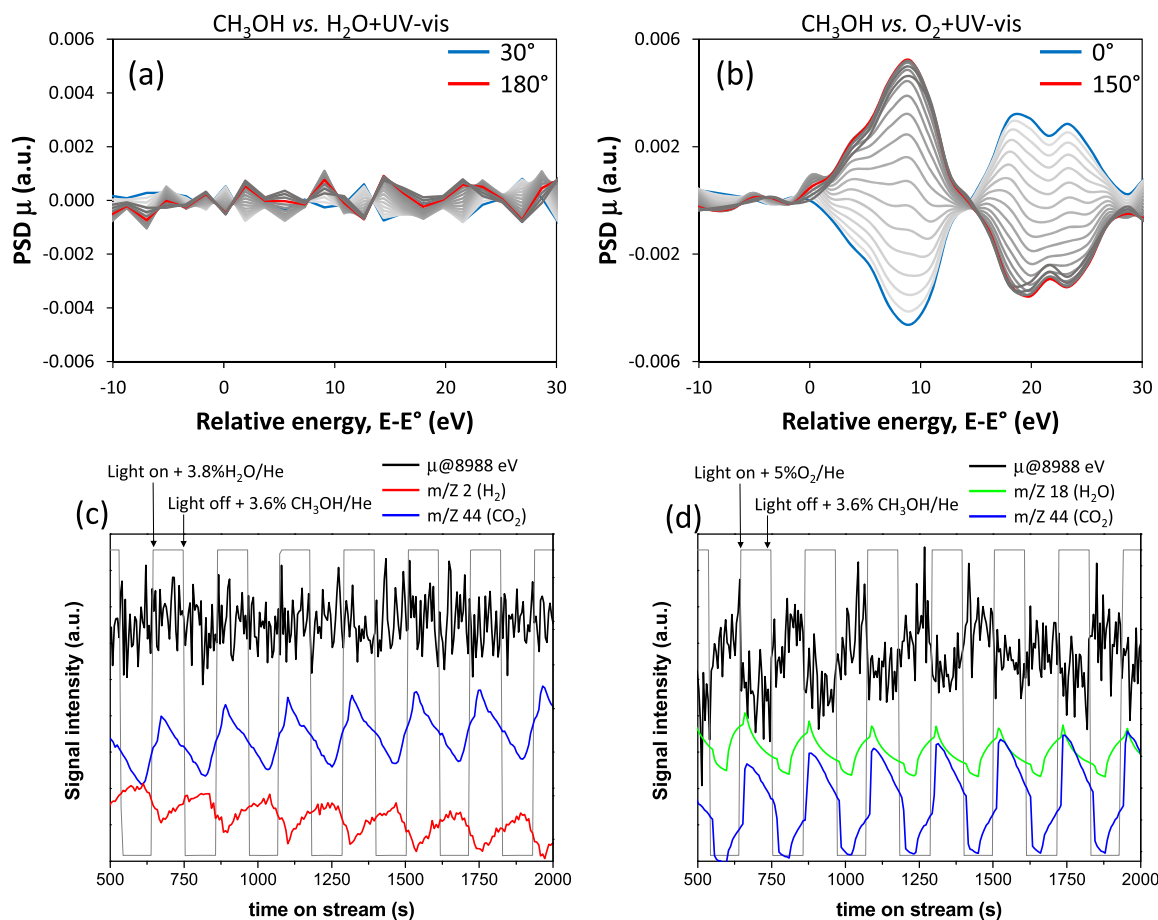


Figure 7. ME-XANES results at the Cu K-edge obtained over the FP-2Cu/TiO₂ sample. (a,b) Phase-resolved spectra in the $0^\circ < \varphi^{\text{PSD}} < 180^\circ$ range and (c,d) time-on-stream variation of the mass spectrometer *m/z* signals of H₂ (red line), CO₂ (blue lines), and H₂O (green line) and of XAS absorption (μ , black lines) at 8988 eV for the (a,c) CH₃OH vs H₂O + UV–vis and (b,d) CH₃OH vs O₂ + UV–vis modulation experiments.

accompanied by an increase of the white line intensity, respectively. Both these spectrum variations are in full agreement with a periodic reduction of Cu(II) to Cu(I). Figure 7d shows the time variation of μ at 8988 eV due to the periodic Cu(II) reduction to Cu(I) together with the variation of the mass spectrometer m/z signals corresponding to CO_2 and H_2O . Under UV–vis irradiation in an oxygen atmosphere, the XAS absorption μ at 8988 eV periodically decreases, indicating an oxidation of Cu(I) to Cu(II) accompanied by CO_2 and H_2O evolution due to the reaction of methanol adsorbed on TiO_2 with O_2 and VB holes. Although the ME-XAS experiment reveals Cu(II)/Cu(I) switching, the above-presented results of photocatalytic tests showed that FP-Cu/ TiO_2 is significantly less performing than bare FP- TiO_2 . Hence, the possible catalytic path involving the Cu(II)/Cu(I) switching seems to be less efficient than the direct photocatalytic oxidation of methanol on the bare FP- TiO_2 surface. Indeed, IFCT is a very effective mechanism for promoting photocatalytic reactions over atomically dispersed copper as that obtained by grafting.^{12,64} In the case of Cu NPs, IFCT may occur at the Cu– TiO_2 interface only. The rather high copper loading on TiO_2 employed in the present work leads to the formation of relatively large Cu NPs that hinder IFCT and cover part of the active TiO_2 surface, hampering photon absorption and methanol reaction with VB holes. The combination of these two drawbacks may explain the lower activity of FP-Cu/ TiO_2 with respect to bare FP- TiO_2 (Table 3).

Finally, very interesting results arise from ME-XAS experiments under *anaerobic* conditions (CH_3OH vs H_2O + light). When steady-state conditions are reached, 70% of copper is reduced to Cu(0) and only 6% residual Cu(II) was revealed by the linear combination fit of the XANES spectra (Table 5). This suggests the formation of metallic Cu core NPs covered by CuO_x shell. Based on ICP results, we found that *ca.* 20% of the Cu could be incorporated within the as-prepared sample. This percentage is anyway lower than the overall amount of oxidized Cu (Cu(II) + Cu(I)) reported in Table 5 of 30%. Thus, even assuming a contribution arising from doped Cu to the XAS spectrum, there would be still residual oxidized Cu that could account for the proposed outer CuO_x shell. Moreover, both demodulated spectra (Figure 7a) and the results of the linear combination analysis (Table 5) evidence that there is no variation of the copper oxidation state or chemical environment during the periodic switch from methanol to water under chopped irradiation. This demonstrates that Cu NPs, unlike Pt NPs, are not the active sites of hydrogen evolution during the methanol photo-steam reforming reaction, at least with the here employed relatively high metal loading. This is not unexpected in consideration of the relatively low work function of copper compared to TiO_2 . Moreover, the CuO_x shell covering the metal Cu core may act as an insulating layer for electron transfer at the Cu surface for hydrogen production. A possible reaction mechanism based on these results is depicted in Figure 8.

In particular, in presence of O_2 , that is, a more oxidizer species than water, Cu(I) is oxidized to Cu(II) and then back to Cu(I) by IFCT together with water formation according to the following reactions

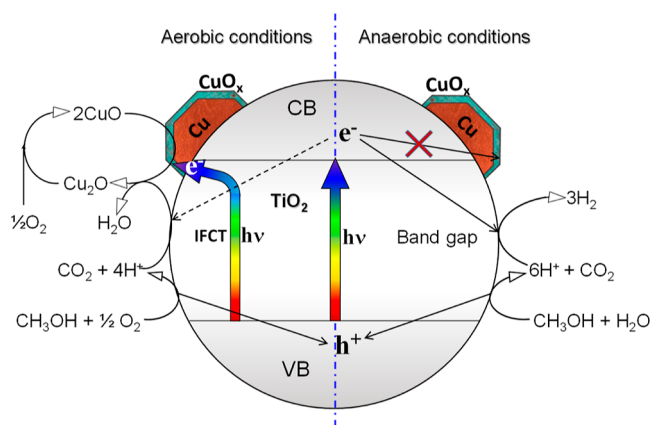
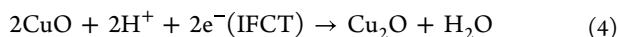


Figure 8. Schematic representation of the mechanism of photocatalytic methanol oxidation under *aerobic* ($\text{CH}_3\text{OH} + \text{O}_2$) and *anaerobic* ($\text{CH}_3\text{OH} + \text{H}_2\text{O}$) conditions over Cu/ TiO_2 , as suggested by ME-XAS results. Under aerobic conditions, IFCT at the Cu– TiO_2 interface may occur.

This mechanism cannot occur under anaerobic conditions due to the absence of a species capable of oxidizing Cu(I) back to Cu(II). Thus, under anaerobic conditions, Cu NPs are not taking part in the photocatalytic mechanism.

4. CONCLUSIONS

ME-XAS demonstrated to be an effective tool to reveal redox dynamics and surface species adsorbed on the active sites of the catalyst under working conditions. Although XAS is intrinsically a bulk technique due to the long penetration depth of hard X-rays, ME-XAS coupled with PSD proved to be able to bring surface sensitivity to XAS. The surface modification of TiO_2 with Pt or Cu NPs, at least at relatively high loading, proved to have opposite effects on the gas-phase photocatalytic oxidation of methanol when performed in the absence or presence of oxygen. Pt confirms to be an effective co-catalyst under *anaerobic* conditions with a significant increase of both CO_2 and H_2 production rates compared to bare TiO_2 , whereas Cu NPs on TiO_2 have only limited effects on the photocatalytic performance. This behavior results from the different ability of Pt and Cu NPs to capture the electrons photo-promoted in the TiO_2 CB, with the consequent decrease of charge carrier recombination. In contrast, both Pt and Cu NPs have detrimental effects in the photocatalytic oxidation of methanol under *aerobic* conditions. ME-XAS demonstrates that both metals on TiO_2 undergo reduction under UV–vis irradiation, under both *aerobic* and *anaerobic* conditions. Furthermore, ME-XAS experiments at the Pt L3-edge provide evidence of the dynamic adsorption of H or O on Pt, which confirms Pt as the active site for H_2 or H_2O evolution under *anaerobic* or *aerobic* conditions, respectively. In contrast, no surface redox dynamics was detected by the ME-XAS experiments at the Cu K-edge under *anaerobic* conditions, demonstrating that Cu is not active as H_2 evolution site, while in the presence of oxygen, a Cu(II)/Cu(I) redox switching was detected, which can assist the water evolution reaction.

AUTHOR INFORMATION

Corresponding Author

Gian Luca Chiarello — Dipartimento di Chimica, Università degli Studi di Milano, I-20133 Milano, Italy; orcid.org/0000-0003-4550-175X; Phone: +39 02 503 14281;

Email: gianluca.chiareello@unimi.it; Fax: +39 02 503 14300

Authors

Massimo Bernareggi – Dipartimento di Chimica, Università degli Studi di Milano, I-20133 Milano, Italy

Elena Selli – Dipartimento di Chimica, Università degli Studi di Milano, I-20133 Milano, Italy; orcid.org/0000-0001-8391-7639

Complete contact information is available at:
<https://pubs.acs.org/10.1021/acscatal.2c03025>

Notes

The authors declare no competing financial interest.

ACKNOWLEDGMENTS

The European Synchrotron Radiation Facility (ESRF, Grenoble, France) is acknowledged for providing the beamtime (proposal Nr, CH-4579) at beamline ID24. The authors are grateful to Dr. Giovanni Agostini and to Dr. Luca Bettini for their help during measurements. This work received financial support from the Ministero dell'Istruzione, dell'Università e della Ricerca (MIUR), PRIN 20179337R7 MULTI-e project.

REFERENCES

- (1) Kumaravel, V.; Mathew, S.; Bartlett, J.; Pillai, S. C. Photocatalytic Hydrogen Production Using Metal Doped TiO₂: A Review of Recent Advances. *Appl. Catal., B* **2019**, *244*, 1021–1064.
- (2) Schneider, J.; Matsuoka, M.; Takeuchi, M.; Zhang, J.; Horiuchi, Y.; Anpo, M.; Bahnemann, D. W. Understanding TiO₂ Photocatalysis: Mechanisms and Materials. *Chem. Rev.* **2014**, *114*, 9919–9986.
- (3) Chiarello, G. L.; Aguirre, M. H.; Selli, E. Hydrogen Production by Photocatalytic Steam Reforming of Methanol on Noble Metal-Modified TiO₂. *J. Catal.* **2010**, *273*, 182–190.
- (4) Khan, M. R.; Chuan, T. W.; Yousuf, A.; Chowdhury, M. N. K.; Cheng, C. K. Schottky Barrier and Surface Plasmonic Resonance Phenomena towards the Photocatalytic Reaction: Study of Their Mechanisms to Enhance Photocatalytic Activity. *Catal. Sci. Technol.* **2015**, *5*, 2522–2531.
- (5) Chiarello, G. L.; Dozzi, M. V.; Scavini, M.; Grunwaldt, J.-D.; Selli, E. One Step Flame-Made Fluorinated Pt/TiO₂ Photocatalysts for Hydrogen Production. *Appl. Catal., B* **2014**, *160–161*, 144–151.
- (6) Ahmed, L. M.; Ivanova, I.; Hussein, F. H.; Bahnemann, D. W. Role of Platinum Deposited on TiO₂ in Photocatalytic Methanol Oxidation and Dehydrogenation Reactions. *Int. J. Photoenergy* **2014**, *2014*, 503516.
- (7) Denny, F.; Scott, J.; Chiang, K.; Teoh, W. Y.; Amal, R. Insight towards the Role of Platinum in the Photocatalytic Mineralisation of Organic Compounds. *J. Mol. Catal. A: Chem.* **2007**, *263*, 93–102.
- (8) Murcia, J. J.; Hidalgo, M. C.; Navio, J. A.; Vaiano, V.; Sannino, D.; Ciambelli, P. Cyclohexane Photocatalytic Oxidation on Pt/TiO₂ Catalysts. *Catal. Today* **2013**, *209*, 164–169.
- (9) Lee, J.; Choi, W. Photocatalytic Reactivity of Surface Platinized TiO₂: Substrate Specificity and the Effect of Pt Oxidation State. *J. Phys. Chem. B* **2005**, *109*, 7399–7406.
- (10) Dozzi, M. V.; Chiarello, G. L.; Pedroni, M.; Livraghi, S.; Giamello, E.; Selli, E. High Photocatalytic Hydrogen Production on Cu(II) Pre-Grafted Pt/TiO₂. *Appl. Catal., B* **2017**, *209*, 417–428.
- (11) Polliotto, V.; Livraghi, S.; Krukowska, A.; Dozzi, M. V.; Zaleska-Medynska, A.; Selli, E.; Giamello, E. Copper-Modified TiO₂ and ZrTiO₄: Cu Oxidation State Evolution during Photocatalytic Hydrogen Production. *ACS Appl. Mater. Interfaces* **2018**, *10*, 27745–27756.
- (12) Irie, H.; Kamiya, K.; Shibamura, T.; Miura, S.; Tryk, D. A.; Yokoyama, T.; Hashimoto, K. Visible Light-Sensitive Cu(II)-Grafted TiO₂ Photocatalysts: Activities and X-Ray Absorption Fine Structure Analyses. *J. Phys. Chem. C* **2009**, *113*, 10761–10766.
- (13) Caudillo-Flores, U.; Muñoz-Batista, M. J.; Kubacka, A.; Fernández-García, M. Operando Spectroscopy in Photocatalysis. *ChemPhotoChem* **2018**, *2*, 777–785.
- (14) Dong, C.-L.; Vayssieres, L. In Situ/Operando X-Ray Spectroscopies for Advanced Investigation of Energy Materials. *Chem.—Eur. J.* **2018**, *24*, 18356–18373.
- (15) El-Roz, M.; Bazin, P.; Daturi, M.; Thibault-Starzyk, F. Operando Infrared (IR) Coupled to Steady-State Isotopic Transient Kinetic Analysis (SSITKA) for Photocatalysis: Reactivity and Mechanistic Studies. *ACS Catal.* **2013**, *3*, 2790–2798.
- (16) El-Roz, M.; Kus, M.; Cool, P.; Thibault-Starzyk, F. New Operando IR Technique to Study the Photocatalytic Activity and Selectivity of TiO₂ Nanotubes in Air Purification: Influence of Temperature, UV Intensity, and VOC Concentration. *J. Phys. Chem. C* **2012**, *116*, 13252–13263.
- (17) Ternero-Hidalgo, J. J.; Guerrero-Pérez, M. O.; Rodríguez-Mirasol, J.; Cordero, T.; Bañares, M. A.; Portela, R.; Bazin, P.; Clet, G.; Daturi, M. Operando Reactor-Cell with Simultaneous Transmission FTIR and Raman Characterization (IR Raman) for the Study of Gas-Phase Reactions with Solid Catalysts. *Anal. Chem.* **2020**, *92*, 5100–5106.
- (18) Hernández-Alonso, M. D.; García-Rodríguez, S.; Suárez, S.; Portela, R.; Sánchez, B.; Coronado, J. M. Operando DRIFTS Study of the Role of Hydroxyl Groups in Trichloroethylene Photo-Oxidation over Titanate and TiO₂ Nanostructures. *Catal. Today* **2013**, *206*, 32–39.
- (19) Wang, K.; Cao, M.; Lu, J.; Lu, Y.; Lau, C. H.; Zheng, Y.; Fan, X. Operando DRIFTS-MS Investigation on Plasmon-Thermal Coupling Mechanism of CO₂ Hydrogenation on Au/TiO₂: The Enhanced Generation of Oxygen Vacancies. *Appl. Catal., B* **2021**, *296*, 120341.
- (20) Chiarello, G. L.; Lu, Y.; Agote-Arán, M.; Pellegrini, R.; Ferri, D. Changes of Pd Oxidation State in Pd/Al₂O₃ Catalysts Using Modulated Excitation DRIFTS. *Catalysts* **2021**, *11*, 116.
- (21) Zhou, Y.; Doronkin, D. E.; Zhao, Z.; Plessow, P. N.; Jelic, J.; Detlefs, B.; Pruessmann, T.; Studt, F.; Grunwaldt, J.-D. Photothermal Catalysis over Nonplasmonic Pt/TiO₂ Studied by Operando HERFD-XANES, Resonant XES, and DRIFTS. *ACS Catal.* **2018**, *8*, 11398–11406.
- (22) Chiarello, G. L.; Nachtegaal, M.; Marchionni, V.; Quaroni, L.; Ferri, D. Adding Diffuse Reflectance Infrared Fourier Transform Spectroscopy Capability to Extended X-Ray-Absorption Fine Structure in a New Cell to Study Solid Catalysts in Combination with a Modulation Approach. *Rev. Sci. Instrum.* **2014**, *85*, 074102.
- (23) Chiarello, G. L.; Ferri, D.; Selli, E. In Situ Attenuated Total Reflection Infrared Spectroscopy Study of the Photocatalytic Steam Reforming of Methanol on Pt/TiO₂. *Appl. Surf. Sci.* **2018**, *450*, 146–154.
- (24) Wang, X. L.; Liu, W.; Yu, Y. Y.; Song, Y.; Fang, W. Q.; Wei, D.; Gong, X. Q.; Yao, Y. F.; Yang, H. G. Operando NMR Spectroscopic Analysis of Proton Transfer in Heterogeneous Photocatalytic Reactions. *Nat. Commun.* **2016**, *7*, 11918.
- (25) Hess, C. New Advances in Using Raman Spectroscopy for the Characterization of Catalysts and Catalytic Reactions. *Chem. Soc. Rev.* **2021**, *50*, 3519–3564.
- (26) Gaur, A.; Schumann, M.; Raun, K. V.; Stehle, M.; Beato, P.; Jensen, A. D.; Grunwaldt, J.; Høj, M. Operando XAS/XRD and Raman Spectroscopic Study of Structural Changes of the Iron Molybdate Catalyst during Selective Oxidation of Methanol. *ChemCatChem* **2019**, *11*, 4871–4883.
- (27) Piccolo, L.; Afanasiev, P.; Morfin, F.; Len, T.; Dessal, C.; Roussel, J. L.; Aouine, M.; Bourgain, F.; Aguilar-Tapia, A.; Proux, O.; Chen, Y.; Soler, L.; Llorca, J. Operando X-Ray Absorption Spectroscopy Investigation of Photocatalytic Hydrogen Evolution over Ultradispersed Pt/TiO₂ Catalysts. *ACS Catal.* **2020**, *10*, 12696–12705.
- (28) Gaur, A.; Hartmann Dabros, T. M.; Høj, M.; Boubnov, A.; Prüssmann, T.; Jelic, J.; Studt, F.; Jensen, A. D.; Grunwaldt, J.-D.

Probing the Active Sites of MoS₂ Based Hydrotreating Catalysts Using Modulation Excitation Spectroscopy. *ACS Catal.* **2019**, *9*, 2568–2579.

(29) Lu, Y.; Santhosh Kumar, M.; Chiarello, G. L.; Dimopoulos Eggenschwiler, P.; Bach, C.; Weilenmann, M.; Spiteri, A.; Weidenkaff, A.; Ferri, D. Operando XANES Study of Simulated Transient Cycles on a Pd-Only Three-Way Catalyst. *Catal. Commun.* **2013**, *39*, 55–59.

(30) Ferri, D.; Newton, M. A.; Di Michiel, M.; Chiarello, G. L.; Yoon, S.; Lu, Y.; Andrieux, J. Revealing the Dynamic Structure of Complex Solid Catalysts Using Modulated Excitation X-Ray Diffraction. *Angew. Chem., Int. Ed.* **2014**, *53*, 8890–8894.

(31) Iglesias-Juez, A.; Chiarello, G. L.; Patience, G. S.; Guerrero-Pérez, M. O. Experimental Methods in Chemical Engineering: X-ray Absorption Spectroscopy—XAS, XANES, EXAFS. *Can. J. Chem. Eng.* **2022**, *100*, 3–22.

(32) Ramaker, D. E.; Koningsberger, D. C. The Atomic AXAFS and $\Delta\mu$ XANES Techniques as Applied to Heterogeneous Catalysis and Electrocatalysis. *Phys. Chem. Chem. Phys.* **2010**, *12*, 5514.

(33) Ferri, D.; Newton, M. A.; Nachtegaal, M. Modulation Excitation X-Ray Absorption Spectroscopy to Probe Surface Species on Heterogeneous Catalysts. *Top. Catal.* **2011**, *54*, 1070–1078.

(34) Chiarello, G. L.; Ferri, D. Modulated Excitation Extended X-Ray Absorption Fine Structure Spectroscopy. *Phys. Chem. Chem. Phys.* **2015**, *17*, 10579–10591.

(35) Lawley, C.; Tehrani, Z. P.; Clark, A. H.; Safonova, O. V.; Döbeli, M.; Strocov, V. N.; Schmidt, T. J.; Lippert, T.; Nachtegaal, M.; Pergolesi, D. Protagonists and Spectators during Photocatalytic Solar Water Splitting with SrTaO_xN_y Oxynitride. *J. Mater. Chem. A* **2022**, *10*, 2374–2387.

(36) Czioska, S.; Boubnov, A.; Escalera-López, D.; Geppert, J.; Zagalskaya, A.; Röse, P.; Saraçi, E.; Alexandrov, V.; Krewer, U.; Cherevko, S.; Grunwaldt, J.-D. Increased Ir–Ir Interaction in Iridium Oxide during the Oxygen Evolution Reaction at High Potentials Probed by Operando Spectroscopy. *ACS Catal.* **2021**, *11*, 10043–10057.

(37) Urakawa, A.; Bürgi, T.; Baiker, A. Sensitivity Enhancement and Dynamic Behavior Analysis by Modulation Excitation Spectroscopy: Principle and Application in Heterogeneous Catalysis. *Chem. Eng. Sci.* **2008**, *63*, 4902–4909.

(38) Müller, P.; Hermans, I. Applications of Modulation Excitation Spectroscopy in Heterogeneous Catalysis. *Ind. Eng. Chem. Res.* **2017**, *56*, 1123–1136.

(39) Ferri, D.; Newton, M. A.; Di Michiel, M.; Yoon, S.; Chiarello, G. L.; Marchionni, V.; Matam, S. K.; Aguirre, M. H.; Weidenkaff, A.; Wen, F.; Gieshoff, J. Synchrotron High Energy X-Ray Methods Coupled to Phase Sensitive Analysis to Characterize Aging of Solid Catalysts with Enhanced Sensitivity. *Phys. Chem. Chem. Phys.* **2013**, *15*, 8629.

(40) König, C. F. J. J.; van Bokhoven, J. A.; Schildhauer, T. J.; Nachtegaal, M. Quantitative Analysis of Modulated Excitation X-Ray Absorption Spectra: Enhanced Precision of EXAFS Fitting. *J. Phys. Chem. C* **2012**, *116*, 19857–19866.

(41) Eyssler, A.; Kleymenov, E.; Kupferschmid, A.; Nachtegaal, M.; Kumar, M. S.; Hug, P.; Weidenkaff, A.; Ferri, D. Improvement of Catalytic Activity of LaFe_{0.95}Pd_{0.05}O₃ for Methane Oxidation under Transient Conditions. *J. Phys. Chem. C* **2011**, *115*, 1231–1239.

(42) Chiarello, G. L.; Rossetti, I.; Forni, L. Flame-Spray Pyrolysis Preparation of Perovskites for Methane Catalytic Combustion. *J. Catal.* **2005**, *236*, 251–261.

(43) Altomare, A.; Burla, M. C.; Giacovazzo, C.; Guagliardi, A.; Moliterni, A. G. G.; Polidori, G.; Rizzi, R. Quanto: A Rietveld Program for Quantitative Phase Analysis of Polycrystalline Mixtures. *J. Appl. Crystallogr.* **2001**, *34*, 392–397.

(44) Rietveld, H. M. A Profile Refinement Method for Nuclear and Magnetic Structures. *J. Appl. Crystallogr.* **1969**, *2*, 65–71.

(45) Scherrer, P. Estimation of the Size and Internal Structure of Colloidal Particles by Means of Röntgen Rays. *Göttinger Nachrichten Math. Phys.* **1918**, *2*, 96–100.

(46) Chiarello, G. L.; Forni, L.; Selli, E. Photocatalytic Hydrogen Production by Liquid- and Gas-Phase Reforming of CH₃OH over Flame-Made TiO₂ and Au/TiO₂. *Catal. Today* **2009**, *144*, 69–74.

(47) Hong, J.; Zhang, W.; Ren, J.; Xu, R. Photocatalytic Reduction of CO₂: A Brief Review on Product Analysis and Systematic Methods. *Anal. Methods* **2013**, *5*, 1086–1097.

(48) Huang, X.; Cao, T.; Liu, M.; Zhao, G. Synergistic Photoelectrochemical Synthesis of Formate from CO₂ on {121} Hierarchical Co₃O₄. *J. Phys. Chem. C* **2013**, *117*, 26432–26440.

(49) Grunwaldt, J.-D.; Caravati, M.; Hannemann, S.; Baiker, A. X-Ray Absorption Spectroscopy under Reaction Conditions: Suitability of Different Reaction Cells for Combined Catalyst Characterization and Time-Resolved Studies. *Phys. Chem. Chem. Phys.* **2004**, *6*, 3037.

(50) Sahu, M.; Biswas, P. Single-Step Processing of Copper-Doped Titania Nanomaterials in a Flame Aerosol Reactor. *Nanoscale Res. Lett.* **2011**, *6*, 441.

(51) Bernareggi, M.; Dozzi, M. V.; Bettini, L. G.; Ferretti, A. M.; Chiarello, G. L.; Selli, E. Flame-Made Cu/TiO₂ and Cu-Pt/TiO₂ Photocatalysts for Hydrogen Production. *Catalysts* **2017**, *7*, 301.

(52) Colón, G.; Maicu, M.; Hidalgo, M. C.; Navío, J. A. Cu-Doped TiO₂ systems with Improved Photocatalytic Activity. *Appl. Catal., B* **2006**, *67*, 41–51.

(53) Teleki, A.; Bjelobrk, N.; Pratsinis, S. E. Flame-Made Nb- and Cu-Doped TiO₂ Sensors for CO and Ethanol. *Sens. Actuators, B* **2008**, *130*, 449–457.

(54) Irie, H.; Kamiya, K.; Shibamura, T.; Miura, S.; Tryk, D. A.; Yokoyama, T.; Hashimoto, K. Visible Light-Sensitive Cu(II)-Grafted TiO₂ Photocatalysts: Activities and X-Ray Absorption Fine Structure Analyses. *J. Phys. Chem. C* **2009**, *113*, 10761–10766.

(55) Praliaud, H. Surface and Bulk Properties of Cu–ZSM-5 and Cu/Al₂O₃ Solids during Redox Treatments. Correlation with the Selective Reduction of Nitric Oxide by Hydrocarbons. *Appl. Catal., B* **1998**, *16*, 359–374.

(56) Nosaka, Y.; Takahashi, S.; Sakamoto, H.; Nosaka, Y. Reaction Mechanism of Cu(II)-Grafted Visible-Light Responsive TiO₂ and WO₃ Photocatalysts Studied by Means of ESR Spectroscopy and Chemiluminescence Photometry. *J. Phys. Chem. C* **2011**, *115*, 21283–21290.

(57) Zhang, W.; Li, Y.; Zhu, S.; Wang, F. Copper Doping in Titanium Oxide Catalyst Film Prepared by DC Reactive Magnetron Sputtering. *Catal. Today* **2004**, *93–95*, S89–S94.

(58) López, R.; Gómez, R.; Llanos, M. E. Photophysical and Photocatalytic Properties of Nanosized Copper-Doped Titania Sol–Gel Catalysts. *Catal. Today* **2009**, *148*, 103–108.

(59) Teoh, W.; Madler, L.; Amal, R. Inter-Relationship between Pt Oxidation States on TiO₂ and the Photocatalytic Mineralisation of Organic Matters. *J. Catal.* **2007**, *251*, 271–280.

(60) Teliska, M.; O'Grady, W. E.; Ramaker, D. E. Determination of H Adsorption Sites on Pt/C Electrodes in HClO₄ from Pt L₂₃ X-Ray Absorption Spectroscopy. *J. Phys. Chem. B* **2004**, *108*, 2333–2344.

(61) Teliska, M.; O'Grady, W. E.; Ramaker, D. E. Determination of O and OH Adsorption Sites and Coverage in Situ on Pt Electrodes from Pt L₂₃ X-Ray Absorption Spectroscopy. *J. Phys. Chem. B* **2005**, *109*, 8076–8084.

(62) Gao, J.; Meng, Y.; Benton, A.; He, J.; Jacobsohn, L. G.; Tong, J.; Brinkman, K. S. Insights into the Proton Transport Mechanism in TiO₂ Simple Oxides by in Situ Raman Spectroscopy. *ACS Appl. Mater. Interfaces* **2020**, *12*, 38012–38018.

(63) Dozzi, M. V.; Chiarello, G. L.; Selli, E. Effects of Surface Modification on the Photocatalytic Activity of TiO₂. *J. Adv. Oxid. Technol.* **2010**, *13*, 305.

(64) Irie, H.; Miura, S.; Kamiya, K.; Hashimoto, K. Efficient Visible Light-Sensitive Photocatalysts: Grafting Cu(II) Ions onto TiO₂ and WO₃ Photocatalysts. *Chem. Phys. Lett.* **2008**, *457*, 202–205.